arXiv:2107.14361v3 [cond-mat.mes-hall] 10 May 2022

Light-driven Topological and Magnetic Phase Transitions in Thin-layer Antiferromagnets

Martin Rodriguez-Vega,[†] Ze-Xun Lin,[‡,¶] A. Leonardo,[§,‖] A. Ernst,[⊥,#] M. G. Vergniory,[§,@] and Gregory A. Fiete[¶,△]

[†]*Theoretical Division, Los Alamos National Laboratory, Los Alamos, New Mexico 87545, USA*

[‡]*Department of Physics, The University of Texas at Austin, Austin, TX 78712, USA*

[¶]*Department of Physics, Northeastern University, Boston, MA 02115, USA*

[§]*Donostia International Physics Center, Paseo Manuel de Lardizabal 4, 20018 San Sebastian, Spain*

[‖]*Department of Physics, University of the Basque Country UPV/ EHU, Leioa, Spain.*

[⊥]*Institut für Theoretische Physik, Johannes Kepler Universität, A 4040 Linz, Austria*

[#]*Max-Planck-Institut für Mikrostrukturphysik, Weinberg 2, D-06120 Halle, Germany*

[@]*Max Planck Institute for Chemical Physics of Solids, Dresden, D-01187, Germany*

[△]*Department of Physics, Massachusetts Institute of Technology, Cambridge, MA 02139, USA*

E-mail:

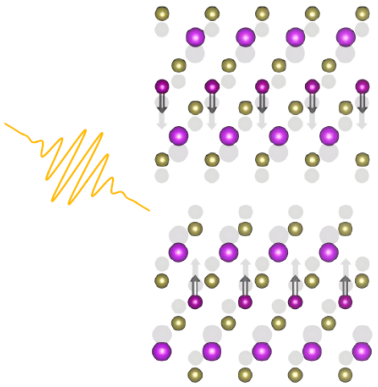
May 12, 2022

Abstract

We theoretically study the effect of low-frequency light pulses in resonance with phonons in the topological and magnetically ordered two septuple-layer (2-SL) $MnBi_2Te_4$

(MBT) and $MnSb_2Te_4$ (MST). These materials share symmetry properties and an antiferromagnetic ground state in pristine form but present different magnetic exchange interactions. In both materials, shear and breathing Raman phonons can be excited via non-linear interactions with photo-excited infrared phonons using intense laser pulses attainable in current experimental setups. The light-induced transient lattice distortions lead to a change in the sign of the effective interlayer exchange interaction and magnetic order accompanied by a topological band transition. Furthermore, we show that moderate anti-site disorder, typically present in MBT and MST samples, can facilitate such an effect. Therefore, our work establishes 2-SL MBT and MST as candidate platforms to achieve non-equilibrium magneto-topological phase transitions.

Graphical TOC Entry



Antiferromagnetic topological insulators (ATIs) can host exotic phases of matter such as the quantum anomalous Hall (QAH) effect and axion insulators.[1] The search for these topological phases motivated the addition of magnetic dopants in topological insulators, which led to the observation of a QAH effect and candidates for axion insulators at very low temperatures.[2–4] However, intrinsic ATIs promise to manifest these phases at higher temperatures, desirable for applications. Indeed, the recent predictions, synthesis and exfoliation of the van der Waals materials $MnBi_2Te_4$, $MnBi_{2n}Te_{3n+1}$, and $MnSb_2Te_4$[5–12] allowed the detection of QAH states in odd septuple layers (SLs), axion states in even SLs ,[13–17] and the observation of an electric-field-induced layer Hall effect in six SL samples.[18]

The intertwined nature of the magnetic and topological order in ATIs offers the possibility to explore topological transitions induced by changes in the magnetic order and vice-versa. For example, recent experiments suggest that increasing the distance between the magnetic planes in the $MnBi_{2n}Te_{3n+1}$ family leads to ferromagnetic order.[8] On the other hand, reducing the distance in $MnBi_2Te_4$ single crystals via hydrostatic pressure leads to the suppression of the AFM order.[19,20] In contrast, in CrI_3 - a low-dimensional magnetic system with trivial topology - hydrostatic pressure induces an antiferromagnet (AFM) to ferromagnet (FM) transition.[21] However, a suitable mechanism to modify the magnetic order in ATIs without applied external magnetic fields or superlattices remains elusive.

To this end, non-equilibrium approaches provide a possible pathway to achieve magneto-topological transitions in ATIs.[22–25] Most notably, non-linear phononics[22,26,27] – a transient and controlled lattice distortion induced by photo-excited phonons– has been successfully used to transiently enhanced superconductivity,[28–30] manipulate and induce ferroelectric states,[31,32] and induce dynamical ferrimagnetic transitions.[33] More recently, A. Stupakiewicz *et al.* induced switching of magnetization in yttrium iron garnet (YIG) thin films by pumping of phonon modes.[34] More generally, light has been shown to induce metastable charge-density-wave states[35] and incite transitions into hidden phases.[36] This experimental evidence motivates the use of non-equilibrium approaches to manipulate magneto-topological order

in ATIs. In this work, we show theoretically that an AFM to FM magnetic transition accompanied by a topological transition can be induced in 2-SL MXT (X=Bi, Sb) samples with intense, experimentally accessible THz laser pulses in resonance with the phonons. Interestingly, the moderate anti-site disorder typically present in these materials reduces the laser intensity threshold to induce the transition.

In MXT materials, the constituent SLs (see Fig. 1(a)) are held together via van der Waals forces, which allows exfoliation in thin samples.[37,38] We will focus on systems with two SLs, since they correspond to the minimal system which can accommodate interlayer AFM order. Within each layer, the magnetic moments are aligned ferromagnetically, but opposite layers posses opposite magnetic moment directions. For 2-SL MBT, the critical temperature is approximately 20 K.[39] For bulk MST, a critical temperature of 19 K has been reported.[40] However, depending on synthesis conditions, bulk MST can posses a ferromagnetic ground state.[41,42]

2-SL MBT and 2-SL MST present space group $P\bar{3}m1$ (No. 164) with point group D_{3d} in their paramagnetic phase. The unit cell contains $N = 14$ atoms with Te atoms located in Wyckoff positions $2d$ $(1/3, 2/3, z)$ and $2c$ $(0, 0, z)$, Mn atoms at $2d$, and X=Bi, Sb atoms in $2c$ and $2d$ positions. The lattice vibration representation is given by $\Gamma_{vib} = 7A_{1g} \oplus 7A_{2u} \oplus 7E_g \oplus 7E_u$, which corresponds to 7 non-degenerate (A_{1g}) and 7 double-degenerate (E_g) Raman modes, with equal number of their infrared counterparts, including the three acoustic modes ($E_u \oplus A_{2u}$). The character table for D_{3d} is shown in the Supporting Information.

Employing group theory and projection operators, we derive the set of real-space displacements which bring the dynamical matrix into block-diagonal form, according to their irreducible representations (see Methods for details). We find that the shear mode where one SL shifts in the [100] direction and the opposite SL in the $[\bar{1}00]$ direction belongs to the E_g irrep. Its partner corresponds to an orthogonal in-plane displacement. The breathing mode consists of the SLs displacing away and towards each other in the direction normal to the plane ([001] and $[00\bar{1}]$ respectively), and belongs to the A_{1g} representation. Fig. 1 (b)

shows representations of these modes. For a detailed group theory study of few-SLs MBT, see Ref. [43]

Now that we have established that the shear and breathing modes are allowed by symmetry, and determined their irreps, we calculate the phonon frequencies at the Γ point. We considered paramagnetic, FM and AFM configurations without spin-orbit coupling and find only negligible differences among the corresponding phonon frequencies. The results for both 2-SL MBT and MST are summarized in Fig. 2. Panels (a) and (b) show the Γ-point phonon frequencies with their corresponding irreducible representation indicated by the shape of the marker. In both materials, the shear and breathing modes present the smallest frequency among the optical modes (indicated by downward gray arrows), and their frequency is smaller by a factor of two compared with the next optical phonon.

Having characterized the properties of the phonons in the harmonic regime, we next consider the symmetry aspects of their non-linear interactions and their laser excitation. A laser pulse incident onto a sample can couple directly with IR modes, depending on the laser frequency and electric field direction. In turn, such an IR mode can couple non-linearly with some Raman modes, provided their irreps satisfy $[\Gamma_{\rm IR} \otimes \Gamma_{\rm IR}] \otimes \Gamma_R \supset A_{1g}$.[27] This mechanism is referred to as non-linear phononics,[26,27,44] and has allowed experimental[22,28–30,32,44,45] and theoretical manipulations of correlated states of matter.[46–49] For the 2-SL MXT's point group, driving a A_{2u} mode can rectify totally-symmetric modes, such as the breading modes, since $A_{2u} \otimes A_{2u} = A_{1g}$. Thus, the shear modes (E_g irrep) are not affected. On the other hand, driving an E_u mode allows coupling with the low-frequency shear modes in conjunction with the breading mode, since $E_u \otimes E_u = A_{1g} \oplus A_{2g} \oplus E_g$.

Once an IR mode has been driven with a strong-enough laser pulse, coupling to all Raman modes with compatible irreps is allowed by symmetry. However, in our case, since the solution of the dynamical equations scale with the inverse square of the Raman frequency ($\sim \Omega_R^{-2}$), we can simplify the calculation and restrict the non-linear interactions to only the low-frequency shear and breathing modes.[27,48] We now consider a laser pulse optimized

to couple with the highest-frequency IR modes, with irrep A_{2u}. This mode presents the strongest coupling with the laser as shown by the largest Born effective charge $\boldsymbol{Z}^*$ [50,51] (see the Supporting Information). In this case, the non-linear potential for 2-SL MBT takes the form

$$V[Q_{IR}, Q_{\mathrm{R}(3)}, t] = \frac{1}{2}\Omega^2_{\mathrm{IR}} Q^2_{\mathrm{IR}} + \frac{1}{2}\Omega^2_{\mathrm{R}(3)} Q^2_{\mathrm{R}(3)} + \gamma_3 Q^2_{\mathrm{IR}} Q_{\mathrm{R}(3)} + \frac{1}{3}\beta_3 Q^3_{\mathrm{R}(3)} + \boldsymbol{Z}^* \cdot \boldsymbol{E_0} \sin(\Omega t) F(t) Q_{\mathrm{IR}}, \tag{1}$$

where γ_3 and β_3 are non-linear coefficients determined from DFT calculations (for the procedure and numerical values, see the Supporting Information), $\boldsymbol{E_0}$ is the electric field amplitude with Gaussian profile $F(t) = \exp\{-t^2/(2\tau^2)\}$, and Ω is the laser frequency, which we choose in resonance with the IR mode $\Omega = \Omega_{IR} = 4.69$ THz. Notice that the driven A_{2u} non-linear potential is much simpler than the one for driven E_u modes. This is because the A_{2u} phonons do not couple to E_g modes up to cubic order interactions.

For 2-SL MST, there are two IR modes with A_{2u} irreps, similar Born effective charge, and frequency. Therefore, we need to consider the simultaneous excitation of the two A_{2u} IR modes which leads to the potential

$$\begin{aligned} V[\{Q_{IR(i)}\}, Q_{\mathrm{R}(3)}, t] &= \sum_{i=1}^{2} \frac{1}{2}\Omega^2_{\mathrm{IR}(i)} Q^2_{\mathrm{IR}(i)} + \frac{1}{2}\Omega^2_{\mathrm{R}(3)} Q^2_{\mathrm{R}(3)} + \\ &\gamma_{1,3} Q^2_{\mathrm{IR}(1)} Q_{\mathrm{R}(3)} + \gamma_{2,3} Q^2_{\mathrm{IR}(2)} Q_{\mathrm{R}(3)} + \gamma_{1,2,3} Q_{\mathrm{IR}(1)} Q_{\mathrm{IR}(2)} Q_{\mathrm{R}(3)} \\ &+ \frac{1}{3}\beta_3 Q^3_{\mathrm{R}(3)} + \left(\boldsymbol{Z_1^*} Q_{\mathrm{IR}(1)} + \boldsymbol{Z_2^*} Q_{\mathrm{IR}(2)}\right) \cdot \boldsymbol{E_0} \sin(\Omega t) F(t). \end{aligned} \tag{2}$$

For 2-SL MST, we consider the laser frequency $\Omega = (\Omega_{IR(1)} + \Omega_{IR(2)})/2$ THz. The phonon dynamics are determined by the equations of motion $\partial_t^2 Q_{\mathrm{R}} = -\partial_{Q_{\mathrm{R}}} V[Q_{\mathrm{IR}(i)}, Q_{\mathrm{R}}]$, $\partial_t^2 Q_{\mathrm{IR}(i)} = -\partial_{Q_{\mathrm{IR}(i)}} V[Q_{\mathrm{IR}(i)}, Q_{\mathrm{R}}]$, where i runs over the driven IR modes. We solve the differential equations numerically. In this work, we do not consider the phonon lifetime. Recent Raman measurements have shown that the lifetime of the breathing mode is approximately 13.3

ps,[52] which is sufficiently long for the electronic degrees of freedom to respond.

The phonon dynamics for a general laser intensity and pulse duration can be obtained by solving the equations of motion numerically. In Fig. 3(a), we show a sketch of a laser-irradiated 2-SL MBT sample. The incoming light with frequency $\Omega = \Omega_{\rm IR} = 4.69$ THz couples directly to the corresponding resonant IR mode. As we show in Fig. 3(b), this mode oscillates around its equilibrium position. Anharmonic coupling induces dynamics in the Raman breathing mode, even though it does not couple directly to the laser. The non-linear nature of the interaction ($\gamma_3 Q_{\rm R} Q_{\rm IR}^2$) leads to oscillations about a position shifted with respect to the equilibrium position. Fig. 3 (c) we shows such oscillations for a laser with peak electric field $E_0 = 0.6$ and pulse duration $\tau = 0.6$ ps. Similar responses are obtained in 2-SL MST, where the main difference is the presence of two A_{2u} IR modes, instead of one. Notice that with light, we can only obtain $\langle Q_{\rm R(3)} \rangle \geq 0$, which corresponds to an effective increase in the Mn-Mn layer separation. This a consequence of the sign of the non-linear coefficients (γ_3 for MBT, $\gamma_{1,3}, \gamma_{2,3}$ for MST)–intrinsic for the materials.

The complementary process of bringing the Mn planes closer to each other could be achieved by applying uniaxial pressure. Theoretically, Ref.[53] predicts that bulk MBT undergoes a topological quantum phase transition under 2.12% compressive strain.

In Fig 3(d), we plot the time average of the shear modes as a function of E_0 for $\tau = 3$ ps. Experimentally, fields of up to 100 MVcm^{-1} have been reported in the range $15-50$ THz[54,55] but limitations are imposed by the amplitude of the corresponding lattice distortion. For 2-SL MBT (2-SL MST) , $\langle Q_{\rm R(3)} \rangle = 5$ Å$/\sqrt{\rm amu}$ correspond to 1.68% (1.88%) increase in the Mn-Mn plane interlayer distance. For 2SL-MST, the dynamical equations become unstable for $E_0 \gtrapprox 2$ MV/cm. However, the range of stability is large enough to obtain a magnetic transition.

Inelastic neutron scattering measurements[56] suggest that the magnetic order in bulk MBT is described by the local-moment Hamiltonian ($S = 5/2$) $\mathcal{H} = \mathcal{H}_{intra} + \mathcal{H}_{inter}$, where the intralayer Hamiltonian can be written as $\mathcal{H}_{intra} = -\sum_{ij} J_{ij} \boldsymbol{S}_i \cdot \boldsymbol{S}_j - D \sum_i (S_i^z)^2$,

with exchange interaction J_{ij} (up to fourth-neighbor interactions are needed to fit the data correctly with $SJ_1 = 0.3$ meV, $SJ_2 = -0.083$ meV, and $SJ_4 = 0.023$ meV), and $SD = 0.12$ meV is a single-ion anisotropy. Thus, the effective intralayer coupling is positive and leads to the ferromagnetic order in each Mn layer. The interlayer Hamiltonian is given by $\mathcal{H}_{inter} = -J_c \sum_{\langle ij \rangle} \boldsymbol{S}_i \cdot \boldsymbol{S}_j$, where experiments suggest a nearest-neighbor AFM interlayer interaction $SJ_c = -0.055$ meV.[56] We obtain the spin Hamiltonian from first-principle calculations, employing a Green's function approach and the magnetic force theorem.[57,58] The calculations were performed using a GGA+U approximation, which describes adequately localized Mn $3d$ states with $U_{eff} = U - J$=5.3 eV.[5,41] For the interlayer interactions, the Hamiltonian takes the more general form $\mathcal{H}_{inter} = -J_c \sum_{ij} \boldsymbol{S}_i \cdot \boldsymbol{S}_j$, where longer-range interactions are relevant. In pristine MXT compounds the interlayer coupling governs the antiferromagnetic order in the ground state, which is mainly mediated by a long-range double exchange interaction via Te ions.[5,41] However, natural lattice defects such as antisite Mn-Bi or Mn-Sb disorder or Mn excess in Bi (Sb) layers can lead to ferromagnetic order in these systems.[41,59]

We now study the effect of laser-induced transient lattice distortions on the magnetic order. Under a time-dependent lattice deformation, small compared with the equilibrium inter-atomic distances, the spin exchange interaction can be approximated as,[60]

$$J[\boldsymbol{u}(t)] = J^0 + \delta J \hat{\boldsymbol{\delta}} \cdot \boldsymbol{u}(t) + \mathcal{O}(\boldsymbol{u}(t)^2), \tag{3}$$

where $\boldsymbol{u}(t)$ is the real-space lattice displacement, J^0 is the equilibrium interaction, and δJ is the coupling constant between the phonon and the spins. The connection with the phonon amplitude Q is given by $\boldsymbol{u}_\kappa = Q/\sqrt{m_\kappa}\boldsymbol{e}_\kappa$, where m_κ is the mass of atom κ, and $\boldsymbol{e}_\kappa$ are the normalized dynamical matrix eigenvectors.

Next, we define the effective spin interaction employing Floquet theory. The exchange interactions set the relevant energy scale, with $\lesssim 1$ meV. Since the infrared phonon frequency

($\Omega_{\rm IR} \approx 4.95, 4.69$ THz) used is larger than the exchange energy, we can define an effective time-averaged exchange interaction $J^{\rm eff} = J^0 + \delta J \hat{\boldsymbol{\delta}} \cdot \langle \boldsymbol{u}_{\rm R} \rangle$, where $\langle \cdots \rangle$ indicates the time average. Thus, when the phonons oscillate about their equilibrium positions (harmonic phonons), such that $\langle \boldsymbol{u} \rangle = 0$, the exchange interactions are not modified in the picture discussed here. The non-zero average shift, however, can renormalize the interactions leading to different magnetic configurations compared with the equilibrium counterparts.

We compute the light-induced effective exchange interactions as a function of the phonon amplitude $Q_{\rm R(3)}$. Our results are summarized in Fig. 4. We plot the average interlayer exchange interaction $\bar{J}_{\rm eff} = 1/\mathcal{N} \sum_{ij} J_{ij}$ as a function of $Q_{\rm R(3)}$. We used a supercell, which consists of seven SLs of MBT (MST) and three SLs of vacuum simulated by empty spheres. $\bar{J}_{\rm eff}$ represents an average exchange interaction, and $\mathcal{N}$ is the number of interacting magnetic moments taken for the average. For pristine 2-SL MBT (2-SL MST), we find a sign change in the interlayer exchange interaction at $Q_{\rm R(3)} \approx 2.4$ Å$\sqrt{\rm amu}$ ($Q_{\rm R(3)} \approx 0.7$ Å$\sqrt{\rm amu}$). These phonon amplitudes can be obtained with a laser pulse with $E_0 \approx 1.7$ MV/cm and $\tau = 0.3$ ps ($E_0 \approx 1.5$ MV/cm and $\tau = 0.3$ ps), as we show in Fig. 3. Generally, increasing the vertical distance between the Mn magnetic moments weakens the antiferromagnetic coupling and favours ferromagnetic order in these systems. The time scale for the spin reorientation following the sign change in $\bar{J}_{\rm eff}$ depends on parameters such as the Gilbert damping factor,[61] the exact spin anisotropy for 2-SL MBT and MST, and the laser-induced $\bar{J}_{\rm eff}$, but are within the limits of the effect we predict to occur.

Since MXT samples are prone to anti-site disorder,[41,59,62–65] with disorder percentages dependent on the sample fabrication process, we also discuss the role of disorder in the light-induced magnetic transition. Depending on concentration percentage, Mn-Sb anti-site disorder can tune the interlayer magnetic interaction into ferromagnetic states.[63] Here, we study theoretically the role of the anti-site disorder in the light-induced magnetic transition discussed in the previous section.

First, we will assume that the anti-site disorder has a negligible effect on the phonon

frequencies. This assumption is supported by recent Raman measurements in 2-SL MBT samples with inherent anti-site disorder, since the measured phonon frequencies are in agreement with density functional calculations for pristine samples.[52]

Next, we introduce disorder in our calculations for the exchange interactions. The anti-site disorder is assumed to be an interchange of Mn with Bi(Sb) elements between the Mn layer and Bi(Sb) layers. This is consistent with recent experiments.[41] Anti-site disorder effects were found to have a quantitatively important effect on the exchange interaction in these materials. Disorder effects are treated using a coherent potential approximation (CPA) as it is implemented within multiple scattering theory.[66] We show our results in Fig. 4, where we consider 5% anti-site disorder, which is a realistic concentration in most of the known MXT samples.[5,41,63] In general, anti-site disorder favors a ferromagnetic interlayer coupling. The main reason for this is that Mn moments in Bi(Sb) layers favour a long-range ferromagnetic coupling between the septuple layers.[67] Also the reduction of magnetic moments in Mn layers diminishes the antiferromagnetic coupling. At zero displacement, a finite amount of disorder can weaken the effective exchange interaction, leading to weaker electric fields necessary to drive the transition. In Fig. 4, the concentration we consider leads to a disorder-induced ferromagnetic ground state.

In the previous sections, we established theoretically the possibility to tune the interlayer magnetic order from antiferromagnetic to ferromagnetic in 2-SL MXT samples using light in resonance with the phonons. In this section, we demonstrate that a topological transition accompanies such a light-induced magnetic transition.

The topology in MBT is rich. In bulk MBT the magnetic structure is invariant with respect to time-reversal and half a lattice translation symmetries. This leads to a $\mathbb{Z}_2$ topological classification, with $\mathbb{Z}_2 = 1$.[5] In the thin-film limit, the topology depends in the number of SLs.[68] For example, 1-SL MBT is predicted to be a FM trivial insulator, with Chern number $C = 0$. 2-SL, 4-SL and 6-SL MBT present a zero plateau QAH, with C=0 in the AFM phase and $|C| = 1$ in the FM phase. Odd-layer (3-, 5- and 7-SL) MBT is predicted to be in a

$|C| = 1$ QAH insulating state. Experimentally, the QAH state has been observed in 5-SL MBT at 1.4 kelvin[37] and a zero Hall plateau -characteristic of an axion insulating state- in 6-SL MBT.[38]

We study the topology of 2-SL MBT as a function of the lattice displacements by examining the electronic band structure and the projection of the p X=Bi, Sb and Te states. The band inversion serves as an indicator of the topological nature of the material within topological band theory.[69] Our results are summarized in Fig. 5. In the equilibrium configuration (left panels with $Q = 0$) with FM order, both 2SL-MBT and 2SL-MST exhibit the expected band inversion.[5,41] For the out-of-equilibrium distorted structures (right panels), FM order is preferred as we showed in the previous sections. We find that the band inversion is present, which indicates the topological nature of the new laser-induced structures.

This work studied the effect of terahertz light pulses in resonance with infrared phonons in the magnetic and topological order of 2-SL MXT samples theoretically. We found that moderate laser intensities, attainable in current experimental setups, can induce non-linear dynamics in the Raman breathing mode. The time-average of these dynamics leads to effective lattice distortions that separate apart the SLs, effectively increasing the distance between magnetic atom planes. Using first-principles methods, we found that the new non-equilibrium lattice configuration can favor ferromagnetic order. Furthermore, the transition between antiferromagnetic and magnetic order can be tuned via anti-site disorder. We showed that the magnetic change is accompanied by a topological transition, as diagnosed by a band inversion as a function of phonon amplitude. Thus, our theoretical work demonstrates the possibility of achieving a sought-after magnetic-topological transition in 2-SL MXT samples experimentally. Such transition in both 2-SL MBT and MST establishes a broader materials trend, which could be applied to other van der Waals magnetic topological materials.

Acknowledgements

We thank Michael Vogl for useful discussions. This research was primarily supported by the National Science Foundation through the Center for Dynamics and Control of Materials: an NSF MRSEC under Cooperative Agreement No. DMR-1720595, with additional support from NSF DMR-1949701 and NSF DMR-2114825. This work was performed in part at the Aspen Center for Physics, which is supported by National Science Foundation grant PHY-1607611. A.L. acknowledges support from the funding grant: PID2019-105488GB-I00. M. R-V. was supported by LANL LDRD Program and by the U.S. Department of Energy, Office of Science, Basic Energy Sciences, Materials Sciences and Engineering Division, Condensed Matter Theory Program. M.G.V. thanks support from the Spanish Ministry of Science and Innovation (grant number PID2019-109905GB-C21) and Deutsche Forschungsgemeinschaft (DFG, German Research Foundation) GA 3314/1-1 – FOR 5249 (QUAST).

Supporting Information Available

Additional details on the group theory phonon symmetry analysis, character table for the crystal point group, phonon first-principles calculations, and a discussion on the single-particle excitation spectrum.

References

(1) Mong, R. S. K.; Essin, A. M.; Moore, J. E. Antiferromagnetic topological insulators. *Phys. Rev. B* **2010**, *81*, 245209.

(2) Chang, C.-Z. et al. Experimental Observation of the Quantum Anomalous Hall Effect in a Magnetic Topological Insulator. *Science* **2013**, *340*, 167.

(3) Mogi, M.; Kawamura, M.; Yoshimi, R.; Tsukazaki, A.; Kozuka, Y.; Shirakawa, N.;

Takahashi, K. S.; Kawasaki, M.; Tokura, Y. A magnetic heterostructure of topological insulators as a candidate for an axion insulator. *Nature Materials* **2017**, *16*, 516–521.

(4) Gooth, J.; Bradlyn, B.; Honnali, S.; Schindler, C.; Kumar, N.; Noky, J.; Qi, Y.; Shekhar, C.; Sun, Y.; Wang, Z.; Bernevig, B. A.; Felser, C. Axionic charge-density wave in the Weyl semimetal (TaSe4)2I. *Nature* **2019**, *575*, 315–319.

(5) Otrokov, M. M. et al. Prediction and observation of an antiferromagnetic topological insulator. *Nature* **2019**, *576*, 416–422.

(6) Gong, Y. et al. Experimental Realization of an Intrinsic Magnetic Topological Insulator. *Chinese Physics Letters* **2019**, *36*, 076801.

(7) Hu, C. et al. A van der Waals antiferromagnetic topological insulator with weak interlayer magnetic coupling. *Nature Commu* **2020**, *11*, 97.

(8) Hu, C. et al. Realization of an intrinsic ferromagnetic topological state in $MnBi_8Te_{13}$. *Sci Adv* **2020**, *6*, eaba4275.

(9) Jahangirli, Z. A.; Alizade, E. H.; Aliev, Z. S.; Otrokov, M. M.; Ismayilova, N. A.; Mammadov, S. N.; Amiraslanov, I. R.; Mamedov, N. T.; Orudjev, G. S.; Babanly, M. B.; Shikin, A. M.; Chulkov, E. V. Electronic structure and dielectric function of Mn-Bi-Te layered compounds. *Journal of Vacuum Science & Technology B* **2019**, *37*, 062910.

(10) Aliev, Z. S.; Amiraslanov, I. R.; Nasonova, D. I.; Shevelkov, A. V.; Abdullayev, N. A.; Jahangirli, Z. A.; Orujlu, E. N.; Otrokov, M. M.; Mamedov, N. T.; Babanly, M. B.; Chulkov, E. V. Novel ternary layered manganese bismuth tellurides of the $MnTe$-Bi_2Te_3 system: Synthesis and crystal structure. *Journal of Alloys and Compounds* **2019**, *789*, 443–450.

(11) Ge, W.; Sass, P. M.; Yan, J.; Lee, S. H.; Mao, Z.; Wu, W. Direct evidence of ferromagnetism in MnSb2Te4. 2021.

(12) Xu, Y.; Elcoro, L.; Song, Z.-D.; Wieder, B. J.; Vergniory, M. G.; Regnault, N.; Chen, Y.; Felser, C.; Bernevig, B. A. High-throughput calculations of magnetic topological materials. *Nature* **2020**, *586*, 702–707.

(13) Liu, C.; Wang, Y.; Li, H.; Wu, Y.; Li, Y.; Li, J.; He, K.; Xu, Y.; Zhang, J.; Wang, Y. Robust axion insulator and Chern insulator phases in a two-dimensional antiferromagnetic topological insulator. *Nature Materials* **2020**,

(14) Deng, Y.; Yu, Y.; Shi, M. Z.; Guo, Z.; Xu, Z.; Wang, J.; Chen, X. H.; Zhang, Y. Quantum anomalous Hall effect in intrinsic magnetic topological insulator $MnBi_2Te_4$. *Science* **2020**, eaax8156.

(15) Ovchinnikov, D. et al. Intertwined Topological and Magnetic Orders in Atomically Thin Chern Insulator MnBi2Te4. *arXiv:2011.00555* **2020**,

(16) Ge, J.; Liu, Y.; Li, J.; Li, H.; Luo, T.; Wu, Y.; Xu, Y.; Wang, J. High-Chern-number and high-temperature quantum Hall effect without Landau levels. *Natl. Sci. Rev.* **2020**, *7*, 1280–1287.

(17) Lüpke, F.; Pham, A. D.; Zhao, Y.-F.; Zhou, L.-J.; Lu, W.; Briggs, E.; Bernholc, J.; Kolmer, M.; Ko, W.; Chang, C.-Z.; Ganesh, P.; Li, A.-P. Local manifestations of thickness dependent topology and axion edge state in topological magnet $MnBi_2Te_4$. 2021.

(18) Gao, A. et al. Layer Hall effect in a 2D topological axion antiferromagnet. *Nature* **2021**, *595*, 521–525.

(19) Chen, K. Y.; Wang, B. S.; Yan, J.-Q.; Parker, D. S.; Zhou, J.-S.; Uwatoko, Y.; Cheng, J.-G. Suppression of the antiferromagnetic metallic state in the pressurized MnBi2Te4 single crystal. *Physical Review Materials* **2019**, *3*.

(20) Pei, C.; Xia, Y.; Wu, J.; Zhao, Y.; Gao, L.; Ying, T.; Gao, B.; Li, N.; Yang, W.; Zhang, D.; Gou, H.; Chen, Y.; Hosono, H.; Li, G.; Qi, Y. Pressure-Induced Topolog-

ical and Structural Phase Transitions in an Antiferromagnetic Topological Insulator. *Chinese Physics Letters* **2020**, *37*, 066401.

(21) Li, T.; Jiang, S.; Sivadas, N.; Wang, Z.; Xu, Y.; Weber, D.; Goldberger, J. E.; Watanabe, K.; Taniguchi, T.; Fennie, C. J.; Fai Mak, K.; Shan, J. Pressure-controlled interlayer magnetism in atomically thin CrI3. *Nature Materials* **2019**, *18*, 1303–1308.

(22) Mankowsky, R.; Först, M.; Cavalleri, A. Non-equilibrium control of complex solids by nonlinear phononics. *Reports on Progress in Physics* **2016**, *79*, 064503.

(23) Oka, T.; Kitamura, S. Floquet Engineering of Quantum Materials. *Annual Review of Condensed Matter Physics* **2019**, *10*, 387–408.

(24) Rudner, M. S.; Lindner, N. H. Band structure engineering and non-equilibrium dynamics in Floquet topological insulators. *Nature Reviews Physics* **2020**, *2*, 229–244.

(25) Rodriguez-Vega, M.; Vogl, M.; Fiete, G. A. Low-frequency and Moiré–Floquet engineering: A review. *Annals of Physics* **2021**, 168434.

(26) Först, M.; Manzoni, C.; Kaiser, S.; Tomioka, Y.; Tokura, Y.; Merlin, R.; Cavalleri, A. Nonlinear phononics as an ultrafast route to lattice control. *Nature Physics* **2011**, *7*, 854.

(27) Subedi, A.; Cavalleri, A.; Georges, A. Theory of nonlinear phononics for coherent light control of solids. *Phys. Rev. B* **2014**, *89*, 220301.

(28) Fausti, D.; Tobey, R. I.; Dean, N.; Kaiser, S.; Dienst, A.; Hoffmann, M. C.; Pyon, S.; Takayama, T.; Takagi, H.; Cavalleri, A. Light-Induced Superconductivity in a Stripe-Ordered Cuprate. *Science* **2011**, *331*, 189–191.

(29) Mankowsky, R. et al. Nonlinear lattice dynamics as a basis for enhanced superconductivity in YBa2Cu3O6.5. *Nature* **2014**, *516*, 71.

(30) Mitrano, M.; Cantaluppi, A.; Nicoletti, D.; Kaiser, S.; Perucchi, A.; Lupi, S.; Di Pietro, P.; Pontiroli, D.; Riccò, M.; Clark, S. R.; Jaksch, D.; Cavalleri, A. Possible light-induced superconductivity in K3C60 at high temperature. *Nature* **2016**, *530*, 46.

(31) Mankowsky, R.; von Hoegen, A.; Först, M.; Cavalleri, A. Ultrafast Reversal of the Ferroelectric Polarization. *Phys. Rev. Lett.* **2017**, *118*, 197601.

(32) Nova, T. F.; Disa, A. S.; Fechner, M.; Cavalleri, A. Metastable ferroelectricity in optically strained SrTiO3. *Science* **2019**, *364*, 1075–1079.

(33) Disa, A. S.; Fechner, M.; Nova, T. F.; Liu, B.; Först, M.; Prabhakaran, D.; Radaelli, P. G.; Cavalleri, A. Polarizing an antiferromagnet by optical engineering of the crystal field. *Nature Physics* **2020**, *16*, 937–941.

(34) Stupakiewicz, A.; Davies, C. S.; Szerenos, K.; Afanasiev, D.; Rabinovich, K. S.; Boris, A. V.; Caviglia, A.; Kimel, A. V.; Kirilyuk, A. Ultrafast phononic switching of magnetization. *Nature Physics* **2021**, *17*, 489–492.

(35) Vaskivskyi, I.; Gospodaric, J.; Brazovskii, S.; Svetin, D.; Sutar, P.; Goreshnik, E.; Mihailovic, I. A.; Mertelj, T.; Mihailovic, D. Controlling the metal-to-insulator relaxation of the metastable hidden quantum state in 1T-TaS2. *Science Advances* **2015**, *1*.

(36) Stojchevska, L.; Vaskivskyi, I.; Mertelj, T.; Kusar, P.; Svetin, D.; Brazovskii, S.; Mihailovic, D. Ultrafast Switching to a Stable Hidden Quantum State in an Electronic Crystal. *Science* **2014**, *344*, 177–180.

(37) Deng, Y.; Yu, Y.; Shi, M. Z.; Guo, Z.; Xu, Z.; Wang, J.; Chen, X. H.; Zhang, Y. Quantum anomalous Hall effect in intrinsic magnetic topological insulator MnBi2Te4. *Science* **2020**, *367*, 895–900.

(38) Liu, C.; Wang, Y.; Li, H.; Wu, Y.; Li, Y.; Li, J.; He, K.; Xu, Y.; Zhang, J.; Wang, Y. Ro-

bust axion insulator and Chern insulator phases in a two-dimensional antiferromagnetic topological insulator. *Nature Materials* **2020**, *19*, 522–527.

(39) Yang, S.; Xu, X.; Zhu, Y.; Niu, R.; Xu, C.; Peng, Y.; Cheng, X.; Jia, X.; Huang, Y.; Xu, X.; Lu, J.; Ye, Y. Odd-Even Layer-Number Effect and Layer-Dependent Magnetic Phase Diagrams in $MnBi_2Te_4$. *Phys. Rev. X* **2021**, *11*, 011003.

(40) Yan, J.-Q.; Okamoto, S.; McGuire, M. A.; May, A. F.; McQueeney, R. J.; Sales, B. C. Evolution of structural, magnetic, and transport properties in $MnBi_{2-x}Sb_xTe_4$. *Phys. Rev. B* **2019**, *100*, 104409.

(41) Wimmer, S. et al. Mn-rich MnSb2Te4: A topological insulator with magnetic gap closing at high Curie temperatures of 45-50 K. 2021.

(42) Ge, W.; Sass, P. M.; Yan, J.; Lee, S. H.; Mao, Z.; Wu, W. Direct evidence of ferromagnetism in $MnSb_2Te_4$. *Phys. Rev. B* **2021**, *103*, 134403.

(43) Rodriguez-Vega, M.; Leonardo, A.; Fiete, G. A. Group theory study of the vibrational modes and magnetic order in the topological antiferromagnet $MnBi_2Te_4$. *Phys. Rev. B* **2020**, *102*, 104102.

(44) Först, M.; Mankowsky, R.; Bromberger, H.; Fritz, D.; Lemke, H.; Zhu, D.; Chollet, M.; Tomioka, Y.; Tokura, Y.; Merlin, R.; Hill, J.; Johnson, S.; Cavalleri, A. Displacive lattice excitation through nonlinear phononics viewed by femtosecond X-ray diffraction. *Solid State Communications* **2013**, *169*, 24–27.

(45) Nova, T. F.; Cartella, A.; Cantaluppi, A.; Först, M.; Bossini, D.; Mikhaylovskiy, R. V.; Kimel, A. V.; Merlin, R.; Cavalleri, A. An effective magnetic field from optically driven phonons. *Nature Physics* **2017**, *13*, 132–136.

(46) Sentef, M. A.; Kemper, A. F.; Georges, A.; Kollath, C. Theory of light-enhanced phonon-mediated superconductivity. *Phys. Rev. B* **2016**, *93*, 144506.

(47) Khalsa, G.; Benedek, N. A. Ultrafast optically induced ferromagnetic/antiferromagnetic phase transition in GdTiO3 from first principles. *npj Quantum Materials* **2018**, *3*, 15.

(48) Juraschek, D. M.; Fechner, M.; Spaldin, N. A. Ultrafast Structure Switching through Nonlinear Phononics. *Phys. Rev. Lett.* **2017**, *118*, 054101.

(49) Rodriguez-Vega, M.; Lin, Z.-X.; Leonardo, A.; Ernst, A.; Chaudhary, G.; Vergniory, M. G.; Fiete, G. A. Phonon-mediated dimensional crossover in bilayer CrI_3. *Phys. Rev. B* **2020**, *102*, 081117.

(50) Gonze, X.; Lee, C. Dynamical matrices, Born effective charges, dielectric permittivity tensors, and interatomic force constants from density-functional perturbation theory. *Phys. Rev. B* **1997**, *55*, 10355–10368.

(51) Baroni, S.; de Gironcoli, S.; Dal Corso, A.; Giannozzi, P. Phonons and related crystal properties from density-functional perturbation theory. *Rev. Mod. Phys.* **2001**, *73*, 515–562.

(52) Choe, J.; Lujan, D.; Rodriguez-Vega, M.; Ye, Z.; Leonardo, A.; Quan, J.; Nunley, T. N.; Chang, L.-J.; Lee, S.-F.; Yan, J.; Fiete, G. A.; He, R.; Li, X. Electron–Phonon and Spin–Lattice Coupling in Atomically Thin Layers of MnBi2Te4. *Nano Letters* **2021**,

(53) Guo, W.-T.; Huang, L.; Yang, Y.; Huang, Z.; Zhang, J.-M. Pressure-induced topological quantum phase transition in the magnetic topological insulator MnBi2Te4. *New Journal of Physics* **2021**,

(54) Sell, A.; Leitenstorfer, A.; Huber, R. Phase-locked generation and field-resolved detection of widely tunable terahertz pulses with amplitudes exceeding 100 MV/cm. *Opt. Lett.* **2008**, *33*, 2767–2769.

(55) Kampfrath, T.; Tanaka, K.; Nelson, K. A. Resonant and nonresonant control over matter and light by intense terahertz transients. *Nature Photonics* **2013**, *7*, 680.

(56) Li, B.; Yan, J.-Q.; Pajerowski, D.; Gordon, E.; Nedić, A.-M.; Sizyuk, Y.; Ke, L.; Orth, P.; Vaknin, D.; McQueeney, R. Competing Magnetic Interactions in the Antiferromagnetic Topological Insulator MnBi2Te4. *Physical Review Letters* **2020**, *124*.

(57) Liechtenstein, A. I.; Katsnelson, M. I.; Antropov, V. P.; Gubanov, V. A. Local spin density functional approach to the theory of exchange interactions in ferromagnetic metals and alloys. *Journal of Magnetism and Magnetic Materials* **1987**, *67*, 65 – 74.

(58) Hoffmann, M.; Ernst, A.; Hergert, W.; Antonov, V. N.; Adeagbo, W. A.; Matthias Geilhufe, R.; Ben Hamed, H. Magnetic and Electronic Properties of Complex Oxides from First-Principles. *physica status solidi (b)* **2020**, *n/a*.

(59) Lai, Y.; Ke, L.; Yan, J.; McDonald, R. D.; McQueeney, R. J. Defect-driven ferrimagnetism and hidden magnetization in MnBi2Te4. *Physical Review B* **2021**, *103*.

(60) Granado, E.; García, A.; Sanjurjo, J. A.; Rettori, C.; Torriani, I.; Prado, F.; Sánchez, R. D.; Caneiro, A.; Oseroff, S. B. Magnetic ordering effects in the Raman spectra of $La_{1-x}Mn_{1-x}O_3$. *Phys. Rev. B* **1999**, *60*, 11879–11882.

(61) Gilbert, T. A phenomenological theory of damping in ferromagnetic materials. *IEEE Transactions on Magnetics* **2004**, *40*, 3443–3449.

(62) Yan, J.-Q.; Zhang, Q.; Heitmann, T.; Huang, Z.; Chen, K. Y.; Cheng, J.-G.; Wu, W.; Vaknin, D.; Sales, B. C.; McQueeney, R. J. Crystal growth and magnetic structure of MnBi2Te4. *Phys. Rev. Materials* **2019**, *3*, 064202.

(63) Liu, Y.; Wang, L.-L.; Zheng, Q.; Huang, Z.; Wang, X.; Chi, M.; Wu, Y.; Chakoumakos, B. C.; McGuire, M. A.; Sales, B. C.; Wu, W.; Yan, J. Site Mixing for Engineering Magnetic Topological Insulators. *Phys. Rev. X* **2021**, *11*, 021033.

(64) Yuan, Y.; Wang, X.; Li, H.; Li, J.; Ji, Y.; Hao, Z.; Wu, Y.; He, K.; Wang, Y.; Xu, Y.; Duan, W.; Li, W.; Xue, Q.-K. Electronic States and Magnetic Response of MnBi2Te4 by Scanning Tunneling Microscopy and Spectroscopy. *Nano Letters* **2020**, *20*, 3271–3277.

(65) Li, H.; Liu, S.; Liu, C.; Zhang, J.; Xu, Y.; Yu, R.; Wu, Y.; Zhang, Y.; Fan, S. Antiferromagnetic topological insulator MnBi2Te4: synthesis and magnetic properties. *Phys. Chem. Chem. Phys.* **2020**, *22*, 556–563.

(66) Gyorffy, B. L. Coherent-Potential Approximation for a Nonoverlapping-Muffin-Tin-Potential Model of Random Substitutional Alloys. *Phys. Rev. B* **1972**, *5*, 2382–2384.

(67) Vergniory, M. G.; Otrokov, M. M.; Thonig, D.; Hoffmann, M.; Maznichenko, I. V.; Geilhufe, M.; Zubizarreta, X.; Ostanin, S.; Marmodoro, A.; Henk, J.; Hergert, W.; Mertig, I.; Chulkov, E. V.; Ernst, A. Exchange interaction and its tuning in magnetic binary chalcogenides. *Phys. Rev. B* **2014**, *89*, 165202.

(68) Otrokov, M.; Rusinov, I.; Blanco-Rey, M.; Hoffmann, M.; Vyazovskaya, A.; Eremeev, S.; Ernst, A.; Echenique, P.; Arnau, A.; Chulkov, E. Unique Thickness-Dependent Properties of the van der Waals Interlayer Antiferromagnet $MnBi_2Te_4$ Films. *Phys. Rev. Lett.* **2019**, *122*, 107202.

(69) Bansil, A.; Lin, H.; Das, T. Colloquium: Topological band theory. *Rev. Mod. Phys.* **2016**, *88*, 021004.

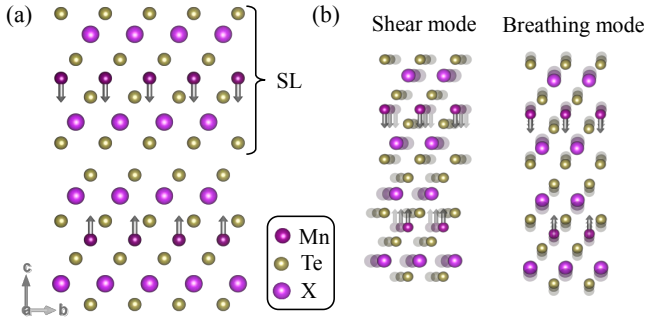


Figure 1: (Color online) (a) 2-SL MXT lattice structure and magnetic order (moments shown in gray arrows). X = Bi, Sb atoms are represented in pink, Te atoms in yellow, and Mn atoms in purple. (b) Low-frequency shear and breathing modes characteristic of few-layer materials. The breathing mode preserves all the crystal symmetries.

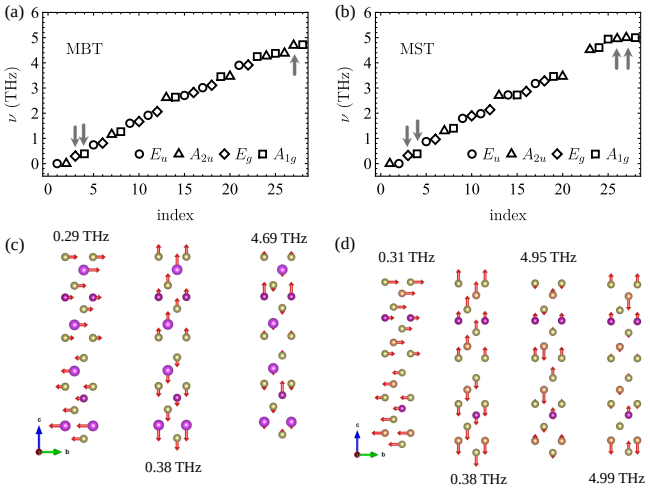


Figure 2: (Color online.) Phonon frequencies for (a) 2-SL MBT and (b) 2-SL MST obtained with first-principles calculations. The gray arrows indicate the phonons illustrated below. In panels (c) and (d) we show the real-space lattice displacements with their corresponding frequencies. Red arrows indicates the displacements.

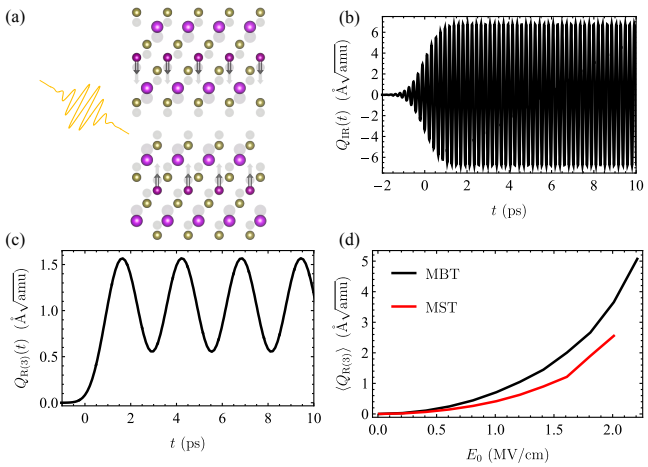


Figure 3: (Color online.) (a) Sketch of a light-induced lattice distortion. (b) Time dependence of the infrared phonon mode directly excited by the incident laser pulse in 2-SL MBT. (c) Non-linearly-excited breathing mode, which oscillates about a new shifted position. The laser parameters used in (b) and (c) are $\tau = 0.6$ ps and $E_0 = 0.6$ MV/cm. (d) Average displacement of the non-linearly photo-excited breathing mode $Q_{\mathrm{R}(3)}$ for MBT (black) and MST (red) for $\tau = 0.3$ ps and laser frequency $\Omega = \Omega_{\mathrm{IR}(1)}$ for 2-SL MBT and $\Omega = (\Omega_{\mathrm{IR}(1)} + \Omega_{\mathrm{IR}(2)})/2$ for 2-SL MST.

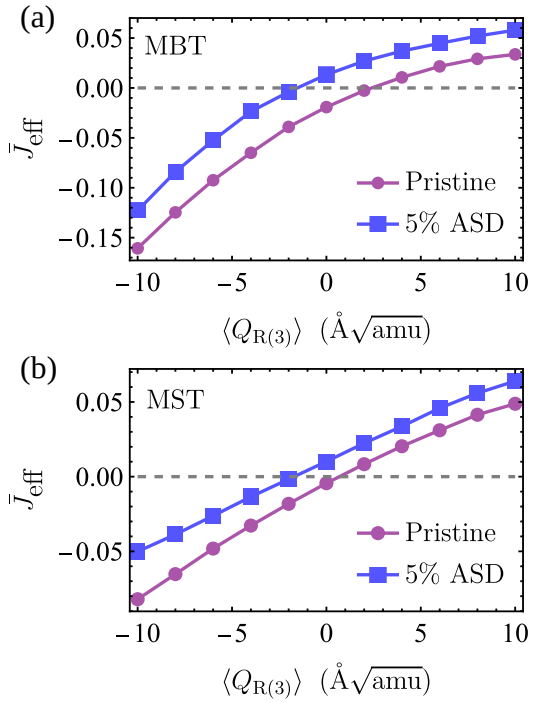


Figure 4: (Color online.) Effective averaged interlayer exchange interaction as a function of the average breathing mode $\langle Q_{\mathrm{R}(3)} \rangle$ for (a) 2SL-MBT and (b) 2SL-MST. The purple circles correspond to pristine samples, while squares correspond to 5% anti-site disorder (ASD).

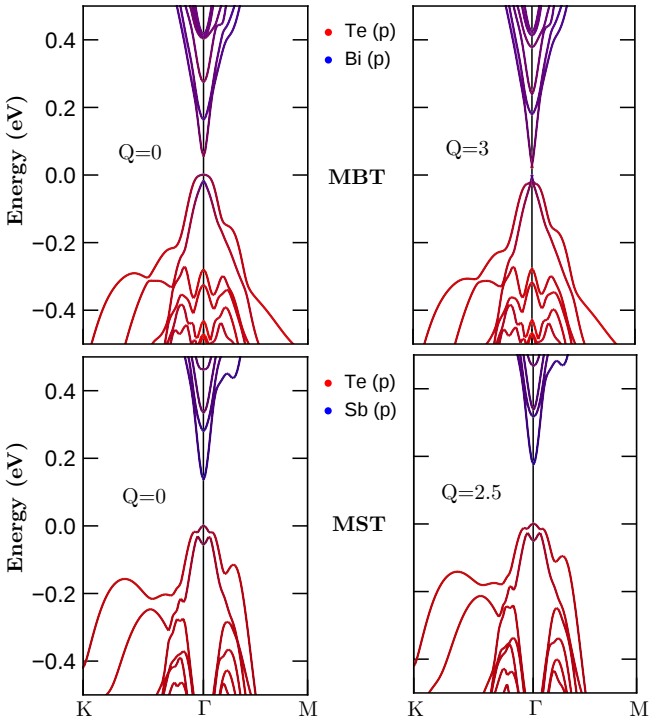


Figure 5: (Color online.) Band structure with projected p states for 2SL-MXT in the FM state. In all cases (FM static ($Q = 0$) and FM out-of-equilibrium ($Q \neq 0$)), we find that the bands are inverted.